DOI: xxx/xxxx

ARTICLE TYPE

Fully decoupled unconditionally stable Crank-Nicolson

leapfrog numerical methods for the Cahn-Hilliard-Darcy

- 4 system
- 5 Yali Gao¹ | Daozhi Han²

Correspondence

13

14

18

19

Corresponding author Daozhi Han. Email: daozhiha@buffalo.edu

Abstract

We develop two totally decoupled, linear and second-order accurate numerical methods that are unconditionally energy stable for solving the Cahn-Hilliard-Darcy equations for two phase flows in porous media or in a Hele-Shaw cell. The implicit-explicit Crank-Nicolson leapfrog method is employed for the discretization of the Cahn-Hilliard equation to obtain linear schemes. Furthermore the artificial compression technique and pressure correction methods are utilized, respectively, so that the Cahn-Hilliard equation and the update of the Darcy pressure can be solved independently. We establish unconditionally long time stability of the schemes. Ample numerical experiments are performed to demonstrate the accuracy and robustness of the numerical methods, including simulations of the Rayleigh-Taylor instability, the Saffman-Taylor instability (fingering phenomenon).

KEYWORDS

Crank-Nicolson leap-frog scheme; second order accuracy; unconditional stability; Cahn-Hilliard-Darcy system; Galerkin finite element method

7 1 INTRODUCTION

Interfaces of multiphase flows in porous media or Hele-Shaw cells are often times unstable. A prominent instability in this setting is the so-called Saffman-Taylor instability which occurs in the displacement a viscous fluid by a less viscous one in porous materials and exhibits fingering patterns—viscous fingering Such phenomena has important applications in oil recovery, infiltration, and many other fields including tumor growth in biomechanics, crystal solidification, electrowetting and polymer liquid crystal techniques. Due to the instability and the resulting topological changes of the interface, classical sharp interface models such as the Muskat problem could be ill-posed. We refrain from reviewing the vast literature in this direction. An alternative relaxation approach is the diffuse interface method leading to models of the Cahn-Hilliard type. Diffuse interface models for two-phase flows in a porous medium could be derived from variational principles [7][8], or from upscaling of the Cahn-Hilliard-(Navier)-Stokes equations [9][9][1][1][2][3]. See also [14][5][6] for derivation of the Cahn-Hilliard-Hele-Shaw system in a Hele-Shaw cell.

In this article we focus on developing efficient and high-order accurate numerical methods for solving the Cahn-Hilliard-Darcy equations (CHD), a popular phase field model for two-phase flows in porous media. The CHD system is a strongly coupled nonlinear system that models interfacial phenomena with sharp transitions in narrow layers (stiffness). There have been abundant numerical works addressing these challenges [17[18]192021222324]. Feng and Wise [21] analyzed a fully discrete implicit finite element method for studying the CHD system, establishing

Journal 2023;00:1–17 wileyonlinelibrary.com/journal/ © 2023 Copyright Holder Name 1

¹School of Mathematics and Statistics, Northwestern Polytechnical University, Xi'an Shaanxi, P.R.China

²Department of Mathematics, The State University of New York at Buffalo, Buffalo, NY, USA

Y. Gao was partially supported by the NSFC, PR China grant 11901461, Natural Science Foundation of Guangdong Province, PR China 2023A1515010697. D. Han is supported by the National Science Foundation grant DMS-2310340.

unconditional unique solvability and convergence of the numerical scheme. Han and Wang proposed a second-order decoupled and unconditionally stable numerical method for solving the CHD system. The key idea for decoupled computation is the pressure correction technique, while second-order convex-concave splitting of the energy potential is utilized for maintaining the energy law. The scheme is however nonlinear requiring nonlinear iterative solvers. In recent years a class of Lagrange multiplier approaches are developed for the design of high-order, unconditionally stable, linear and decoupled time-stepping methods for gradient flow models. Popular methods in this class include the scalar auxiliary variable (SAV) method the invariant energy quadratization (IEQ) method, and many other variants. For the CHD equations Yang constructed a fully-decoupled second-order linear numerical scheme in which zero-energy-contribution idea is introduced to break the coupling of velocity and phase-field variable. Yang and Kim exploited multiple auxiliary variables to conduct a simple and efficient decoupled second-order convergent numerical scheme for numerically simulating the dynamics of the CHD system.

Despite the stability and high efficiency of Lagrange multiplier type approaches, they appear to suffer from poor accuracy in practice, especially for long-time simulations 26. Moreover, the energy law satisfied by these methods is in general in terms of new Lagrange multipliers, hence not a direct approximation of the original energy law. Connecting the two forms of the energy law by post-processing is numerically demonstrated to improve the accuracy of the method^[27]. The goal of this work is to develop a time-marching scheme with the following properties: linear, fully decoupled and second-order accuracy in time, energy stable, easy-to-implement; and to apply the proposed numerical scheme to gain insight into interfacial instability. There are two main ingredients in our design: the combination of Crank-Nicolson and leapfrog time-stepping (CNLF) that gives a linear discretization of the Cahn-Hilliard equation; the artificial compression and pressure projection techniques for incompressible flow leading to decoupled and fast algorithms for the update of Darcy pressure. These strategies have been widely employed in solving the Navier-Stokes equations 28 29, the Stokes-Darcy equations 30, and the Cahn-Hilliard-Navier-Stokes equations 313233. In particular, it is discovered in 32 that the CNLF discretization of the nonlinear term yields a linear second-order accurate unconditionally stable algorithm for the Cahn-Hilliard equation. As far as we know, the CNLF method is the only way to obtain a linear second-order scheme without resorting to extra Lagrange multipliers. It is noted that our scheme does not need the grad-div stabilization in the fluid equations to obtain unconditional stability, in contrast to the case of Navier-Stokes equations. In addition to accuracy and stability tests, we employ the proposed numerical scheme in simulations of Rayleigh-Taylor instability and Saffman-Taylor instability in both two dimensions and three dimensions. The numerical results demonstrate the ability of the numerical method in capturing details of droplet splitting, the onset and evolution of viscous fingering.

The rest of this work are organized as follows. In Section 2 we provide the Cahn-Hilliard-Darcy model. In Section 3 we present the second-order time-stepping methods and analyze their unconditional stability. In section 4, we introduce the fully discrete schemes with finite element method for spatial discretization. In Section 5, ample numerical experiments are reported to illustrate the accuracy and robustness of developed numerical method. Finally, a brief summary is concluded in the last section.

2 | THE MODEL EQUATIONS

25

26

27

29

30

31

33

35

37

43

45

47

48

49

50

51

52

53

54

55

57

The dimensionless form of the Cahn-Hilliard-Darcy equations is as following [1917]

$$\frac{ReDa}{\chi} \frac{\partial \mathbf{u}}{\partial t} + \nu(\phi) \Pi^{-1} \mathbf{u} = -\nabla p - \frac{\epsilon^{-1}}{We} \phi \nabla \mu, \tag{2.1a}$$

$$\nabla \cdot \mathbf{u} = 0, \tag{2.1b}$$

$$\chi \frac{\partial \phi}{\partial t} + \nabla \cdot (\phi \mathbf{u}) = \frac{1}{Pe} \nabla \cdot (m(\phi) \nabla \mu), \tag{2.1c}$$

$$\mu = (\phi^3 - \phi) - \epsilon^2 \Delta \phi, \tag{2.1d}$$

where u is the fluid velocity, p is the pressure, ϕ is the order parameter taking values ± 1 in the bulk of each phase, respectively, μ is the chemical potential. Here Re represents Reynold'd number, Da is the Darcy number, ϵ measures thickness of the transition layer between the two phases, Pe is the diffusion Peclet number, ν is the viscosity, ρ_0 is

the density, Π is the permeability matrix, χ is the porosity, We is the ratio of modified capillary number to Darcy number, m is the mobility. Throughout, we assume $\nu(\phi)$ and $m(\phi)$ are bounded below and above, i.e.,

$$0 < \nu_1 \le \nu(\phi) \le \nu_2, \quad 0 < m_1 \le m(\phi) \le m_2.$$
 (2.2)

When $\frac{ReDa}{\chi}$ is small, one often neglects the transient effect in the flow field. In this study we take into account of the transient effects. The time derivative of the fluid velocity is necessary for the design of second-order decoupled

time-stepping method, though the method also works for non-transient CHD albeit without decoupling. We note

that the CHD system (2.1) is closely related to the Cahn-Hilliard-Hele-Shaw system (2.1)

Equipped with the following initial and boundary conditions

$$\mathbf{u} \cdot \mathbf{n} = 0$$
, on $\partial \Omega \times (0, T)$ (2.3a)

$$\nabla \phi \cdot \mathbf{n} = \nabla \mu \cdot \mathbf{n} = 0, \quad \text{on } \partial \Omega \times (0, T)$$
 (2.3b)

$$(\boldsymbol{u}, \phi)|_{t=0} = (\boldsymbol{u}_0, \phi_0), \quad \text{in } \Omega.$$
 (2.3c)

one can show that the system (2.1) satisfies an energy law:

$$\frac{d}{dt}E(\phi) = -\int_{\Omega} \nu(\phi)\Pi^{-1}|\mathbf{u}|^2 \,d\mathbf{x} - \frac{\epsilon^{-1}}{WePe} \int_{\Omega} m(\phi)|\nabla \mu|^2 \,d\mathbf{x},\tag{2.4}$$

where the free energy functional E is defined as

$$E(\phi) = ReDa \int_{\Omega} \frac{1}{2\chi} |\mathbf{u}|^2 d\mathbf{x} + \frac{\chi}{We} \int_{\Omega} \left(\frac{1}{\epsilon} F(\phi) + \frac{\epsilon}{2} |\nabla \phi|^2 \right) d\mathbf{x}, \tag{2.5}$$

with $F(\phi) = \frac{1}{4}(\phi^2 - 1)^2$.

65 3 SECOND-ORDER TIME MARCHING METHODS

In this section we present the semi-discrete time-marching schemes that are discrete in time and continuous in space. Borrowing the idea of Crank-Nicolson leap-frog (CNLF) method, we design two numerical schemes incorporated with the artificial compression and pressure projection method, respectively, and analyze their unconditionally energy stability.

Let (\cdot, \cdot) and $\|\cdot\|$ denote the usual L^2 inner product and norm. Let $0 = t_0 < t_1 < \cdots < t_N = T$ be a uniform partition of [0, T] into subintervals $J^n = (t_n, t_{n+1}), n = 0, 1, \dots, N-1$, with time step size $\Delta t = t_{n+1} - t_n = \frac{T}{N}$.

3.1 The time-stepping scheme based on artificial compression approximation

In order to break the coupling of phase field variables and pressure saving computation cost, we adopt the following artificial compression approximation of the divergence-free condition

$$\nabla \cdot \boldsymbol{u} = \delta \Delta p_t, \tag{3.1}$$

with a small constant $\delta \ (\approx \Delta t^2)$.

The semi-discrete CNLF-AC scheme for solving the system (2.1) is: given ϕ^{n-1} , ϕ^n , u^{n-1} , and p^{n-1} , find the solution ϕ^{n+1} , μ^n , u^{n+1} , p^{n+1} such that

$$\chi \frac{\phi^{n+1} - \phi^{n-1}}{2\Delta t} + \nabla \cdot \left(\phi^n \frac{\boldsymbol{u}^{n+1} + \boldsymbol{u}^{n-1}}{2}\right) - \frac{1}{Pe} \nabla \cdot (m(\phi^n) \nabla \mu^n) = 0, \tag{3.2a}$$

$$\mu^{n} - (\phi^{n})^{2} \frac{\phi^{n+1} + \phi^{n-1}}{2} + \phi^{n} + \epsilon^{2} \frac{\Delta \phi^{n+1} + \Delta \phi^{n-1}}{2} = 0,$$
(3.2b)

$$\frac{ReDa}{\gamma} \frac{u^{n+1} - u^{n-1}}{2\Delta t} + \nu(\phi^n) \Pi^{-1} \frac{u^{n+1} + u^{n-1}}{2} + \nabla p^n + \frac{\epsilon^{-1}}{We} \phi^n \nabla \mu^n = 0,$$
 (3.2c)

$$\alpha \Delta t \Delta (p^{n+1} - p^{n-1}) - \nabla \cdot \boldsymbol{u}^n = 0, \tag{3.2d}$$

where α is a user-specified stabilization parameter.

Remark 1. Through Eq. (3.2c) one can express the velocity u^{n+1} in terms of p^n and ϕ^n , i.e.

$$\boldsymbol{u}^{n+1} = \left(\beta_1 - \beta_2 \nu \Pi^{-1}\right) \boldsymbol{u}^{n-1} - 2\beta_2 \left(\nabla p^n + \frac{\epsilon^{-1}}{We} \phi^n \nabla \mu^n\right).$$

Upon substitution, we can derive the equivalent formulation of (3.2a),

$$\frac{\phi^{n+1} - \phi^{n-1}}{2\Delta t} + \nabla \cdot \left(\phi^n (\beta_1 \mathbf{u}^{n-1} - \beta_2 \nabla p^n)\right) - \nabla \cdot (\bar{m}(\phi^n) \nabla \mu^n) = 0, \tag{3.3}$$

where

$$\beta_{1}(\phi^{n}) = \frac{ReDa}{ReDa + \chi \Delta t \nu(\phi^{n})\Pi^{-1}},$$

$$\beta_{2}(\phi^{n}) = \frac{\chi \Delta t}{ReDa + \chi \Delta t \nu(\phi^{n})\Pi^{-1}},$$

$$\bar{m}(\phi^{n}) = \frac{1}{Pe}m(\phi^{n}) + \beta_{2}\frac{\epsilon^{-1}}{We}(\phi^{n})^{2}.$$
(3.4)

Then, one can solve the Cahn-Hilliard equations (3.2a)-(3.2b) independently. Finally one solves the pressure Poisson equation (3.2d). Therefore the scheme is a completely decoupled algorithm.

Next we show that the scheme is unconditionally stable.

Theorem 1. With $\alpha \geq \frac{2\chi}{ReDa}$, the CNLF-AC scheme (3.2) is unconditionally stable, and the following stability estimate holds for $N \geq 2$

$$\begin{split} \frac{ReDa}{8\chi}(\|\boldsymbol{u}^{N}\|^{2} + \|\boldsymbol{u}^{N-1}\|^{2}) + \frac{\chi}{4We} \left[\frac{1}{\epsilon} \|\phi^{N}\phi^{N-1}\|^{2} + \epsilon(\|\nabla\phi^{N}\|^{2} + \|\nabla\phi^{N-1}\|^{2}) \right] + \frac{\chi\Delta t^{2}}{2ReDa} \left[\|\nabla p^{N}\|^{2} + \|\nabla p^{N-1}\|^{2} \right] \\ & \leq \frac{ReDa}{4\chi} \left[\|\boldsymbol{u}^{1}\|^{2} + \|\boldsymbol{u}^{0}\|^{2} \right] + \frac{\chi}{4We} \left[\frac{1}{\epsilon} \|\phi^{1}\phi^{0}\|^{2} + \epsilon \left(\|\nabla\phi^{1}\|^{2} + \|\nabla\phi^{0}\|^{2} \right) \right] + \frac{\alpha\Delta t^{2}}{2} \left[\|\nabla p^{1}\|^{2} + \|\nabla p^{0}\|^{2} \right] \\ & + \frac{\Delta t}{2} \left[(\boldsymbol{u}^{1}, \nabla p^{0}) - (\boldsymbol{u}^{0}, \nabla p^{1}) \right] - \frac{\epsilon^{-1}\Delta t}{PeWe} \sum_{n=1}^{N-1} \|\sqrt{m(\phi^{n})}\nabla\mu^{n}\|^{2} - \frac{\Pi^{-1}\Delta t}{4} \sum_{n=1}^{N-1} \|\sqrt{\nu(\phi^{n})}(\boldsymbol{u}^{n+1} + \boldsymbol{u}^{n-1})\|^{2}. \end{split} \tag{3.5}$$

Proof. Since

$$\left((\phi^n)^2 \frac{\phi^{n+1} + \phi^{n-1}}{2} - \phi^n \right) \frac{\phi^{n+1} - \phi^{n-1}}{2} = \frac{1}{4} \left[(\phi^{n+1})^2 (\phi^n)^2 - (\phi^n)^2 (\phi^{n-1})^2 - 2\phi^{n+1} \phi^n + 2\phi^n \phi^{n-1} \right]
= \frac{1}{4} \left[(\phi^{n+1} \phi^n - 1)^2 - (\phi^n \phi^{n-1} - 1)^2 \right],$$
(3.6)

multiplying (3.2a) and (3.2b) with test function $\Delta t \frac{\epsilon^{-1}}{We} \mu^n$ and $-\frac{\chi \epsilon^{-1}}{We} \frac{\phi^{n+1} - \phi^{n-1}}{2}$ respectively, integrating and performing integration by parts, adding the resultants together, one obtains

$$\frac{\chi}{4We} \left[\frac{1}{\epsilon} \left(\|\phi^{n+1}\phi^n - 1\|^2 - \|\phi^n\phi^{n-1} - 1\|^2 \right) + \epsilon (\|\nabla\phi^{n+1}\|^2 + \|\nabla\phi^n\|^2) - \epsilon (\|\nabla\phi^n\|^2 + \|\nabla\phi^{n-1}\|^2) \right]
+ \frac{\epsilon^{-1}}{PeWe} \Delta t \|\sqrt{m(\phi^n)} \nabla \mu^n\|^2 - \frac{\epsilon^{-1} \Delta t}{2We} \left(\phi^n (\boldsymbol{u}^{n+1} + \boldsymbol{u}^{n-1}), \nabla \mu^n \right) = 0.$$
(3.7)

Likewise, testing (3.2c) with $\Delta t \frac{u^{n+1} + u^{n-1}}{2}$ and (3.2d) with $-\Delta t \frac{p^{n+1} + p^{n-1}}{2}$, performing integration by parts, one obtains by combining the results

$$\begin{split} \frac{ReDa}{4\chi} \left[(\|\boldsymbol{u}^{n+1}\|^2 + \|\boldsymbol{u}^n\|^2) - (\|\boldsymbol{u}^n\|^2 + \|\boldsymbol{u}^{n-1}\|^2) \right] + \frac{\alpha\Delta t^2}{2} \left[(\|\nabla p^{n+1}\|^2 + \|\nabla p^n\|^2) - (\|\nabla p^n\|^2 + \|\nabla p^{n-1}\|^2) \right] \\ &= -\frac{1}{4}\Pi^{-1}\Delta t \|\sqrt{\nu(\phi^n)}(\boldsymbol{u}^{n+1} + \boldsymbol{u}^{n-1})\|^2 - \frac{\epsilon^{-1}\Delta t}{2We} \left(\phi^n \nabla \mu^n, \boldsymbol{u}^{n+1} + \boldsymbol{u}^{n-1}\right) \\ &+ \frac{\Delta t}{2} \left\{ \left[(\nabla p^{n+1}, \boldsymbol{u}^n) - (\nabla p^n, \boldsymbol{u}^{n-1}) \right] - \left[(\boldsymbol{u}^{n+1}, \nabla p^n) - (\boldsymbol{u}^n, \nabla p^{n-1}) \right] \right\}. \end{split}$$
(3.8)

Adding (3.8) to (3.7), we obtain

$$\begin{split} \frac{ReDa}{4\chi} & \left[(\| \mathbf{u}^{n+1} \|^2 + \| \mathbf{u}^n \|^2) - (\| \mathbf{u}^n \|^2 + \| \mathbf{u}^{n-1} \|^2) \right] + \frac{\alpha \Delta t^2}{2} \left[(\| \nabla p^{n+1} \|^2 + \| \nabla p^n \|^2) - (\| \nabla p^n \|^2 + \| \nabla p^{n-1} \|^2) \right] \\ & + \frac{\chi}{4We} \left[\frac{1}{\epsilon} \left(\| \phi^{n+1} \phi^n - 1 \|^2 - \| \phi^n \phi^{n-1} - 1 \|^2 \right) + \epsilon (\| \nabla \phi^{n+1} \|^2 + \| \nabla \phi^n \|^2) - \epsilon (\| \nabla \phi^n \|^2 + \| \nabla \phi^{n-1} \|^2) \right] \\ & = -\frac{\epsilon^{-1} \Delta t}{PeWe} \| \sqrt{m(\phi^n)} \nabla \mu^n \|^2 - \frac{\Pi^{-1} \Delta t}{4} \| \sqrt{\nu(\phi^n)} (\mathbf{u}^{n+1} + \mathbf{u}^{n-1}) \|^2 \\ & + \frac{\Delta t}{2} \{ [(\nabla p^{n+1}, \mathbf{u}^n) - (\nabla p^n, \mathbf{u}^{n-1})] - [(\mathbf{u}^{n+1}, \nabla p^n) - (\mathbf{u}^n, \nabla p^{n-1})] \}. \end{split} \tag{3.9}$$

Taking summation over n = 1 to n = N - 1, one derives

$$\begin{split} \frac{ReDa}{4\chi}(\|\boldsymbol{u}^{N}\|^{2} + \|\boldsymbol{u}^{N-1}\|^{2}) + \frac{\chi}{4We} \left[\frac{1}{\epsilon} \|\phi^{N}\phi^{N-1} - 1\|^{2} + \epsilon \left(\|\nabla\phi^{N}\|^{2} + \|\nabla\phi^{N-1}\|^{2} \right) \right] + \frac{\alpha\Delta t^{2}}{2} \left[\|\nabla p^{N}\|^{2} + \|\nabla p^{N-1}\|^{2} \right] \\ &= \frac{ReDa}{4\chi} (\|\boldsymbol{u}^{1}\|^{2} + \|\boldsymbol{u}^{0}\|^{2}) + \frac{\chi}{4We} \left[\frac{1}{\epsilon} \|\phi^{1}\phi^{0} - 1\|^{2} + \epsilon \left(\|\nabla\phi^{1}\|^{2} + \|\nabla\phi^{0}\|^{2} \right) \right] + \frac{\alpha\Delta t^{2}}{2} \left[\|\nabla p^{1}\|^{2} + \|\nabla p^{0}\|^{2} \right] \\ &- \frac{\epsilon^{-1}\Delta t}{PeWe} \sum_{n=1}^{N-1} \|\sqrt{m(\phi^{n})}\nabla\mu^{n}\|^{2} - \frac{\Pi^{-1}\Delta t}{4} \sum_{n=1}^{N-1} \|\sqrt{\nu(\phi^{n})}(\boldsymbol{u}^{n+1} + \boldsymbol{u}^{n-1})\|^{2} \\ &+ \frac{\Delta t}{2} [(\boldsymbol{u}^{1}, \nabla p^{0}) - (\boldsymbol{u}^{0}, \nabla p^{1})] + \frac{\Delta t}{2} [(\nabla p^{N}, \boldsymbol{u}^{N-1}) - (\nabla p^{N-1}, \boldsymbol{u}^{N})]. \end{split} \tag{3.10}$$

To conclude, one applies Cauchy-Schwartz inequality to the last two terms in (3.10)

$$\frac{\Delta t}{2} \left| (\nabla p^N, \mathbf{u}^{N-1}) - (\nabla p^{N-1}, \mathbf{u}^N) \right| \leq \frac{ReDa}{8\chi} \left[\|\mathbf{u}^N\|^2 + \|\mathbf{u}^{N-1}\|^2 \right] + \frac{\chi \Delta t^2}{2ReDa} \left[\|\nabla p^N\|^2 + \|\nabla p^{N-1}\|^2 \right].$$

Hence by taking $\alpha \ge \frac{2\chi}{ReDa}$, one obtains (3.5). This completes the proof.

The time-stepping scheme based on pressure projection

The numerical scheme (3.2) is totally decoupled and unconditionally stable rather than obeying the energy law of the original system. To design the second-order numerical scheme with energy law, we introduce the second-order pressure projection strategy (1939)40[41] to decouple the velocity and pressure in Darcy equation. In this subsection, we

develop an alternative second-order decoupled CNLF scheme that satisfies the discrete energy dissipation law.

The semi-discrete CNLF-PR scheme for solving the system (2,1) is: given ϕ^{n-1} ϕ^n u^{n-1} and v^{n-1} find the solution

The semi-disctre CNLF-PR scheme for solving the system (2.1) is: given ϕ^{n-1} , ϕ^n , \boldsymbol{u}^{n-1} , and p^{n-1} , find the solution ϕ^{n+1} , μ^n , \boldsymbol{u}^{n+1} , p^{n+1} such that

$$\chi \frac{\phi^{n+1} - \phi^{n-1}}{2\Delta t} + \nabla \cdot \left(\phi^n \frac{\bar{u}^{n+1} + u^{n-1}}{2}\right) - \frac{1}{Pe} \nabla \cdot (m(\phi^n) \nabla \mu^n) = 0, \tag{3.11a}$$

$$\mu^{n} - (\phi^{n})^{2} \frac{\phi^{n+1} + \phi^{n-1}}{2} + \phi^{n} + \epsilon^{2} \frac{\Delta \phi^{n+1} + \Delta \phi^{n-1}}{2} = 0, \tag{3.11b}$$

$$\frac{ReDa}{\chi} \frac{\bar{\boldsymbol{u}}^{n+1} - \boldsymbol{u}^{n-1}}{2\Delta t} + \nu(\phi^n) \Pi^{-1} \frac{\bar{\boldsymbol{u}}^{n+1} + \boldsymbol{u}^{n-1}}{2} + \nabla p^{n-1} + \frac{\epsilon^{-1}}{We} \phi^n \nabla \mu^n = 0, \tag{3.11c}$$

$$\frac{ReDa}{\chi} \frac{u^{n+1} - \bar{u}^{n+1}}{2\Delta t} + \frac{1}{2} \nabla \left(p^{n+1} - p^{n-1} \right) = 0, \tag{3.11d}$$

$$\nabla \cdot \boldsymbol{u}^{n+1} = 0. \tag{3.11e}$$

Remark 2. We remark here that Canh-Hiilliard equation (3.11a)-(3.11b) and Darcy equation (3.11c) can be solved separately since that the intermediate velocity \bar{u}^{n+1} can be expressed explicitly by u^{n-1} , p^{n-1} and ϕ^n , i.e.

$$\bar{\boldsymbol{u}}^{n+1} = (\beta_1 - \nu \Pi^{-1} \beta_2) \boldsymbol{u}^{n-1} - 2\beta_2 (\nabla p^{n-1} + \frac{\epsilon^{-1}}{We} \phi^n \nabla \mu^n). \tag{3.12}$$

In order to eliminate intermediate variable \bar{u}^{n+1} , we substitute (3.12) into (3.11a) and (3.11d), then rewritten the numerical scheme (3.11) as the equivalent formulation

$$\xi \frac{\phi^{n+1} - \phi^{n-1}}{2\Delta t} + \nabla \cdot \left(\phi^n (\beta_1 \boldsymbol{u}^{n-1} - \beta_2 \nabla p^{n-1})\right) - \nabla \cdot (\bar{\boldsymbol{m}}(\phi^n) \nabla \mu^n) = 0, \tag{3.13a}$$

$$\mu^{n} - (\phi^{n})^{2} \frac{\phi^{n+1} + \phi^{n-1}}{2} + \phi^{n} + \epsilon^{2} \frac{\Delta \phi^{n+1} + \Delta \phi^{n-1}}{2} = 0,$$
(3.13b)

$$\frac{ReDa}{2\chi\Delta t}\boldsymbol{u}^{n+1} + \frac{1}{2}\nabla\left(p^{n+1} - p^{n-1}\right) - \frac{ReDa}{2\chi\Delta t}\left(\beta_1 - \nu\Pi^{-1}\beta_2\right)\boldsymbol{u}^{n-1} + \frac{ReDa}{\chi\Delta t}\beta_2\left(\nabla p^{n-1} + \frac{\epsilon^{-1}}{We}\phi^n\nabla\mu^n\right) = 0, \quad (3.13c)$$

$$\nabla \cdot \boldsymbol{u}^{n+1} = 0, \tag{3.13d}$$

where $\beta_1(\phi^n)$, $\beta_2(\phi^n)$ and $\bar{m}(\phi^n)$ are defined as in (3.4). It can clearly observe that the numerical scheme does not involve intermediate velocity \bar{u}^{n+1} , so there is no need to compute the intermediate variable in implementation. Moreover, one can decouple the velocity and pressure by utilizing divergence-free condition (3.13d) for (3.13c). Therefore, the presented CNLF-PR numerical scheme is totally decoupled in separately solving ϕ^{n+1} , μ^n , u^{n+1} , and p^{n+1} .

The CNLF-PR scheme is totally decoupled, and unconditionally stable.

Theorem 2. The CNLF-PR scheme (3.11) is unconditionally stable, namely, the solution ϕ^{n+1} , μ^n , u^{n+1} , p^{n+1} satisfies the following energy dissipation law, for $n \ge 2$

$$\mathcal{E}^{n+1} - \mathcal{E}^{n} \le -\frac{\epsilon^{-1} \Delta t}{P_{e} W_{e}} \| \sqrt{m(\phi^{n})} \nabla \mu^{n} \|^{2} - \frac{\Pi^{-1} \Delta t}{4} \| \sqrt{\nu(\phi^{n})} (\boldsymbol{u}^{n-1} + \bar{\boldsymbol{u}}^{n+1}) \|^{2}. \tag{3.14}$$

with modified discrete energy law \mathcal{E}^{n+1} defined as

$$\mathcal{E}^{n+1} = \frac{ReDa}{4\chi} \left[\|\boldsymbol{u}^{n+1}\|^2 + \|\boldsymbol{u}^n\|^2 \right] + \frac{\chi}{4We} \left[\frac{1}{\epsilon} \|\phi^{n+1}\phi^n - 1\|^2 + \epsilon \left(\|\nabla\phi^{n+1}\|^2 + \|\nabla\phi^n\|^2 \right) \right] + \frac{\chi \Delta t^2}{2ReDa} \left[\|\nabla p^{n+1}\|^2 + \|\nabla p^n\|^2 \right]. \tag{3.15}$$

Proof. Taking the L^2 inner product of (3.11a) and (3.11b) with $\Delta t \frac{\epsilon^{-1}}{We} \mu^n$ and $-\frac{\chi \epsilon^{-1}}{We} \frac{\phi^{n+1} - \phi^{n-1}}{2}$ respectively, performing integration by parts, adding the resultants, using (3.6), one obtains

$$\frac{\chi}{4We} \left[\frac{1}{\epsilon} \left(\|\phi^{n+1}\phi^n - 1\|^2 - \|\phi^n\phi^{n-1} - 1\|^2 \right) + \epsilon \left(\|\nabla\phi^{n+1}\|^2 + \|\nabla\phi^n\|^2 \right) - \epsilon \left(\|\nabla\phi^n\|^2 + \|\nabla\phi^{n-1}\|^2 \right) \right]
+ \frac{\epsilon^{-1}}{PeWe} \Delta t \|\sqrt{m(\phi^n)} \nabla \mu^n\|^2 - \frac{\epsilon^{-1}}{2We} \Delta t \left(\phi^n(\bar{\boldsymbol{u}}^{n+1} + \boldsymbol{u}^{n-1}), \nabla \mu^n \right) = 0.$$
(3.16)

Multiplying (3.11c) with test function $\frac{\Delta t}{2}(\bar{u}^{n+1} + u^{n-1})$, and integrating, we obtain

$$\begin{split} \frac{ReDa}{4\chi} [\|\bar{\boldsymbol{u}}^{n+1}\|^2 - \|\boldsymbol{u}^{n-1}\|^2] + \frac{1}{4}\Pi^{-1}\Delta t\|\sqrt{\nu(\phi^n)}(\boldsymbol{u}^{n-1} + \bar{\boldsymbol{u}}^{n+1})\|^2 + \frac{\epsilon^{-1}}{2We}\Delta t\Big(\phi^n\nabla\mu^n, \bar{\boldsymbol{u}}^{n+1} + \boldsymbol{u}^{n-1}\Big) \\ + \frac{\Delta t}{2} \Big(\nabla p^{n-1}, \bar{\boldsymbol{u}}^{n+1} + \boldsymbol{u}^{n-1}\Big) &= 0. \end{split} \tag{3.17}$$

Now we deal with the last term $(\nabla p^{n-1}, \bar{\boldsymbol{u}}^{n+1} + \boldsymbol{u}^{n-1})$ in (3.17). Taking the inner product of (3.11d) with $\frac{\chi}{ReDa} \Delta t^2 \nabla p^{n-1}$, applying integration by parts, divergence-free condition (3.11e) for \boldsymbol{u}^{n+1} and \boldsymbol{u}^{n-1} , and equality $2b(a-b) = a^2 - b^2 - (a-b)^2$, we derive

$$-\frac{\Delta t}{2} \left(\bar{\boldsymbol{u}}^{n+1} + \boldsymbol{u}^{n-1}, \nabla p^{n-1} \right) + \frac{\chi \Delta t^2}{4ReDa} \left[\|\nabla p^{n+1}\|^2 - \|\nabla p^{n-1}\|^2 - \|\nabla (p^{n+1} - p^{n-1})\|^2 \right] = 0. \tag{3.18}$$

By testing (3.11d) with $\nabla(p^{n+1}-p^{n-1})$ and applying Cauchy-Schwarz inequality, one obtains

$$\frac{\chi}{4ReDa}\Delta t^2 \|\nabla(p^{n+1} - p^{n-1})\|^2 \le \frac{ReDa}{4\chi} \|\boldsymbol{u}^{n+1} - \bar{\boldsymbol{u}}^{n+1}\|^2. \tag{3.19}$$

Taking L^2 inner product of (3.11d) with $2\Delta t \nabla u^{n+1}$, exploiting (3.11e) and $2a(a-b) = a^2 - b^2 + (a-b)^2$, we get

$$\frac{ReDa}{4\chi} \left[\|\boldsymbol{u}^{n+1}\|^2 - \|\bar{\boldsymbol{u}}^{n+1}\|^2 + \|\boldsymbol{u}^{n+1} - \bar{\boldsymbol{u}}^{n+1}\|^2 \right] = 0. \tag{3.20}$$

We add (3.17), (3.18), (3.19) and (3.20) together to obtain

$$\frac{ReDa}{4\chi} \left[\left(\|\boldsymbol{u}^{n+1}\|^2 + \|\boldsymbol{u}^{n}\|^2 \right) - \left(\|\boldsymbol{u}^{n}\|^2 + \|\boldsymbol{u}^{n-1}\|^2 \right) \right] + \frac{\chi \Delta t^2}{4ReDa} \left[\left(\|\nabla p^{n+1}\|^2 + \|\nabla p^{n}\|^2 \right) - \left(\|\nabla p^{n}\|^2 + \|\nabla p^{n-1}\|^2 \right) \right] \\
+ \frac{\Pi^{-1}\Delta t}{4} \|\sqrt{\nu(\phi^n)} (\boldsymbol{u}^{n-1} + \bar{\boldsymbol{u}}^{n+1}) \|^2 + \frac{\epsilon^{-1}}{2We} \Delta t (\phi^n \nabla \mu^n, \bar{\boldsymbol{u}}^{n+1} + \boldsymbol{u}^{n-1}) \le 0. \tag{3.21}$$

Summing up (3.16) and (3.21), we obtain the modified energy law (3.14). Thus we complete the proof of Theorem \Box

4 | FULLY DISCRETE NUMERICAL SCHEMES

In this section, we further discretize the space by continuous Galerkin finite element method for semi-discrete scheme (3.2) and (3.11).

Let \Im_h be a quasi-uniform regular partition of the triangular element with mesh size h. We introduce the finite element spaces $\mathbf{X}_h \subset \mathbf{L}^2$, $Y_h \subset H^1(\Omega)$, $Q_h := Y_h \cap L_0^2(\Omega)$ with $L_0^2(\Omega)$ the L^2 subspace whose elements are of mean zero. Furthermore, We assume that, $\nabla Y_h \subset \mathbf{X}_h$, and \mathbf{X}_h and Q_h satisfy the inf-sup condition for the divergence operator. Then, we construct the totally decoupled fully discretization CNLF-AC and CNLF-PR schemes as follows.

Algorithm 1: CNLF-AC scheme

95

97

98

99

100 101 Assuming that $(\boldsymbol{u}_h^{n-1}, \boldsymbol{u}_h^n, p_h^{n-1}, p_h^n, \phi_h^{n-1}, \phi_h^n)$ are given for $n \ge 1$, we compute $(\boldsymbol{u}_h^{n+1}, p_h^{n+1}, \phi_h^{n+1}, \mu_h^n)$ by the following steps.

Step 1: Find $(\phi_h^{n+1}, \mu_h^n) \in Y_h \times Y_h$, such that

$$\chi\left(\frac{\phi_h^{n+1} - \phi_h^{n-1}}{2\Delta t}, \psi_h\right) - \left(\phi_h^n(\beta_1 \boldsymbol{u}_h^{n-1} - \beta_2 \nabla p_h^n), \nabla \psi_h\right) + \left(\bar{m}(\phi_h^n) \nabla \mu_h^n, \nabla \psi_h\right) = 0, \ \forall \, \psi_h \in Y_h, \tag{4.1}$$

$$(\mu_h^n, \omega_h) - \epsilon^2 \left(\nabla \frac{\phi_h^{n+1} + \phi_h^{n-1}}{2}, \nabla \omega_h \right) - \left((\phi_h^n)^2 \frac{\phi_h^{n+1} + \phi_h^{n-1}}{2}, \omega_h \right) + (\phi_h^n, \omega_h) = 0, \ \forall \, \omega_h \in Y_h, \tag{4.2}$$

where $\beta_1(\phi_h^n)$, $\beta_2(\phi_h^n)$ and $\bar{m}(\phi^n)$ are defined as

$$\beta_{1}(\phi_{h}^{n}) = \frac{ReDa}{ReDa + \chi \Delta t \nu(\phi_{h}^{n})\Pi^{-1}},$$

$$\beta_{2}(\phi_{h}^{n}) = \frac{\chi \Delta t}{ReDa + \chi \Delta t \nu(\phi_{h}^{n})\Pi^{-1}},$$

$$\bar{m}(\phi_{h}^{n}) = \frac{1}{Pe} m(\phi_{h}^{n}) + \beta_{2} \frac{\epsilon^{-1}}{We} (\phi_{h}^{n})^{2}.$$

$$(4.3)$$

Step 2: Find $p_h^{n+1} \in Q_h$, such that

$$\alpha \Delta t \Big(\nabla (p_h^{n+1} - p_h^{n-1}), \nabla q_h \Big) - (\boldsymbol{u}_h^n, \nabla q_h) = 0, \ \forall \ q_h \in Y_h.$$

$$(4.4)$$

Step 3: Find $\boldsymbol{u}_h^{n+1} \in \mathbf{X}_h$, such that

$$\frac{ReDa}{\chi}\left(\frac{\boldsymbol{u}_{h}^{n+1}-\boldsymbol{u}_{h}^{n-1}}{2\Delta t},\boldsymbol{v}_{h}\right)+\Pi^{-1}\left(\nu(\phi_{h}^{n})\frac{\boldsymbol{u}_{h}^{n+1}+\boldsymbol{u}_{h}^{n-1}}{2},\boldsymbol{v}_{h}\right)+\left(\nabla p_{h}^{n},\boldsymbol{v}_{h}\right)+\frac{\epsilon^{-1}}{We}\left(\phi_{h}^{n}\nabla\mu_{h}^{n},\boldsymbol{v}_{h}\right)=0,\ \forall\,\boldsymbol{v}_{h}\in\mathbf{X}_{h}.\tag{4.5}$$

Algorithm 2: CNLF-PR scheme

102

103

106

107

108

109

110

112

Assuming that $(\boldsymbol{u}_h^{n-1}, p_h^{n-1}, p_h^n, \phi_h^{n-1}, \phi_h^n)$ are given for $n \ge 1$, we compute $(\boldsymbol{u}_h^{n+1}, p_h^{n+1}, \phi_h^{n+1}, \mu_h^n)$ by the following steps.

Step 1: Find $(\phi_h^{n+1}, \mu_h^n) \in Y_h \times Y_h$, such that

$$\chi\left(\frac{\phi_h^{n+1} - \phi_h^{n-1}}{2\Delta t}, \psi_h\right) - \left(\phi_h^n(\beta_1 \boldsymbol{u}_h^{n-1} - \beta_2 \nabla p_h^n), \nabla \psi_h\right) + \left(\bar{m}(\phi_h^n) \nabla \mu_h^n, \nabla \psi_h\right) = 0, \ \forall \, \psi_h \in Y_h, \tag{4.6}$$

$$\left(\mu_h^n, \omega_h\right) - \epsilon^2 \left(\nabla \frac{\phi_h^{n+1} + \phi_h^{n-1}}{2}, \nabla \omega_h\right) - \left((\phi_h^n)^2 \frac{\phi_h^{n+1} + \phi_h^{n-1}}{2}, \omega_h\right) + \left(\phi_h^n, \omega_h\right) = 0, \ \forall \, \omega_h \in Y_h, \tag{4.7}$$

where β_1 , β_2 and \bar{m} are given in (4.3).

Step 2: Find $p_h^{n+1} \in Q_h$, such that

$$\frac{1}{2} \left(\nabla \left(p_h^{n+1} - p_h^{n-1} \right), \nabla q_h \right) - \frac{ReDa}{2\chi \Delta t} \left(\left(\beta_1 - \nu \Pi^{-1} \beta_2 \right) \boldsymbol{u}_h^{n-1}, \nabla q_h \right) + \frac{ReDa}{\chi \Delta t} \left(\beta_2 (\nabla p_h^{n-1} + \frac{\epsilon^{-1}}{We} \phi_h^n \nabla \mu_h^n), \nabla q_h \right) = 0, \ \forall \, q_h \in Y_h.$$

$$(4.8)$$

Step 3: Find $\boldsymbol{u}_h^{n+1} \in \mathbf{X}_h$, such that

$$\frac{ReDa}{2\chi\Delta t}\left(\boldsymbol{u}_{h}^{n+1},\boldsymbol{v}_{h}\right) + \frac{1}{2}\left(\nabla\left(p_{h}^{n+1} - p_{h}^{n-1}\right),\boldsymbol{v}_{h}\right) - \frac{ReDa}{2\chi\Delta t}\left(\left(\beta_{1} - \nu\Pi^{-1}\beta_{2}\right)\boldsymbol{u}_{h}^{n-1},\boldsymbol{v}_{h}\right) + \frac{ReDa}{\chi\Delta t}\left(\beta_{2}(\nabla p_{h}^{n-1} + \frac{\epsilon^{-1}}{We}\phi_{h}^{n}\nabla\mu_{h}^{n}),\boldsymbol{v}_{h}\right) = 0, \ \forall \boldsymbol{v}_{h} \in \mathbf{X}_{h}.$$
(4.9)

Remark 3. Both the CNLF-AC scheme and the CNLF-PR scheme can be discretized in space by any classical methods. Following the same argument as the semi-discrete scheme, we note that the CNLF-AC time marching combined with the finite difference method is provably unconditionally stable, while the CNLF-PR method with the finite element spatial discretization (or any other methods) satisfies a similar energy law. Due to the use of substitution of velocity in solving the Cahn-Hilliard equation, we are not able to prove energy stability for the CNLF-AC finite element scheme. In numerical experiments we observe that both time-marching schemes effected with finite element method are stable.

Remark 4. The proposed completely decoupled CNLF-AC and CNLF-PR numerical methods are three-level methods. In order to start this numerical scheme, we need values from the first two steps. The approximation $(\boldsymbol{u}_h^1, p_h^1, \phi_h^1, \mu_h^1)$ should be precomputed in another suitable numerical scheme. For simplicity, we exploited backward Euler method to compute $(\boldsymbol{u}_h^1, p_h^1, \phi_h^1, \mu_h^1)$ during implementation as reported in Section 5.

Remark 5. The developed CNLF-AC scheme (4.1)-(4.5) and CNLF-PR scheme (4.6)-(4.9) are fully decoupled linear algorithms. The existence of solutions is a consequence of uniqueness which is in turned guaranteed by the unconditional energy stability.

Remark 6. We note that error analysis of the CNLF type schemes is a challenge beyond the scope of this work. We defer the error analysis of fully discrete schemes to the future work. We refer to 424343444546 for convergence analysis work on phase field fluid, such as on Cahn-Hilliard-Hlew-Shaw system 2243, Cahn-Hilliard-Stokes-Darcy 44, the magnetohydrodynamics equations 45.

5 NUMERICAL EXPERIMENTS

In this section, we perform several numerical simulations to validate the characteristic features and compatibility of the developed CNLF method for CHD system. We first verify the accuracy and discrete energy stability of the proposed numerical algorithms. Then, we test the spinodal decomposition in ring domain, and interface instability between binary fluids in two- and three-dimension, including interface pinch-off and viscous fingers phenomenon. Moreover, we extend our numerical methods to numerically investigate the rotational Hele-Shaw cell in two and three-dimensional spaces to further validate the good performance of the proposed CNLF method. Throughout, we take Taylor-Hood element for velocity and pressure, and P_2 finite element pairs in two dimensions and P_1 in three dimensions for ϕ_h and μ_h , respectively. The preconditioned conjugate gradient method is used to solve the linear elliptic equation with variable coefficient at each time step.

Example 1: Convergence and accuracy. To illustrate the second-order accuracy in time of CNLF-AC scheme and CNLF-PR scheme, we compute the numerical errors between numerical solutions and accurate solutions on a unit square domain $\Omega = [0,1] \times [0,1]$ for CHD system. Set parameters ReDa, χ , γ , ϵ , m and stabilized parameters α are one. We take the exact solution as follows

$$u(x, y, t) = (-\sin^2(\pi x)\sin(2\pi y)\cos(t), \sin^2(\pi y)\sin(2\pi x)\cos(t)),$$

$$p(x, y, t) = \cos(t)(xy - \frac{1}{4}),$$

$$\phi(x, y, t) = \cos(t)\cos(\pi x)\cos(\pi y).$$

The boundary condition functions and the source terms are chosen from the above exact solution.

The finite element pair $P_2 - P_1 - P_2 - P_2$ is taken for variables u, p, ϕ and μ . The simulation is carried out until T=1.0. The refiner mesh size $h=\frac{1}{128}$ is taken to guarantee that the error arising from spatial discretization is negligible compared to temporal error. Figure 1 displays the L^2 errors at t=1.0 from time step size $\Delta t=\frac{1}{16}$ refining to $\Delta t=\frac{1}{128}$. The numerical results clearly indicate that the proposed CNLF-AC and CNLF-PR schemes provide the expected second-order accuracy in time for all variables.

Example 2: Energy dissipation on a disk domain.

In this test, we numerically simulate the evolution of a "flower" shape droplet to validate the energy dissipation of the developed numerical scheme. The initial conditions are chosen as

$$\phi = -\tanh((\sqrt{(x-0.5)^2 + (y-0.5)^2} - r_1)(\sqrt{2\epsilon}))$$
(5.1)

with $r_1 = 0.25 + 0.1\cos(6\theta)$. We choose parameters $ReDa = 10^{-4}$, $\chi = 1$, $\frac{\nu}{\Pi} = 100$, $\epsilon = 0.02$, We = 100, $\gamma = 0.01$, Pe = 1, m = 0.01, and $\alpha = 2$ on a disk domain with radius 1. The numerical simulation is done up to T = 10.

The dynamical morphology of the phase variable are displayed in Figure 2 under $\Delta t = 0.005$. As shown in Figure 2, the flower firstly gradually evolves into a hexagon, then eventually deforms into a circle driven by surface tension effectively. Figure 3 plots the discrete energy under different time step sizes. One can clearly observe that the numerical scheme satisfies desired energy stability for all presented cases. Moreover, once the energy corresponding to the equilibrium state circle is reached, the energy does not change anymore. It demonstrates that the proposed decoupled numerical is unconditionally long time stable consistently well with the theory results.

Example 3: Spinodal decomposition in ring computational domain.

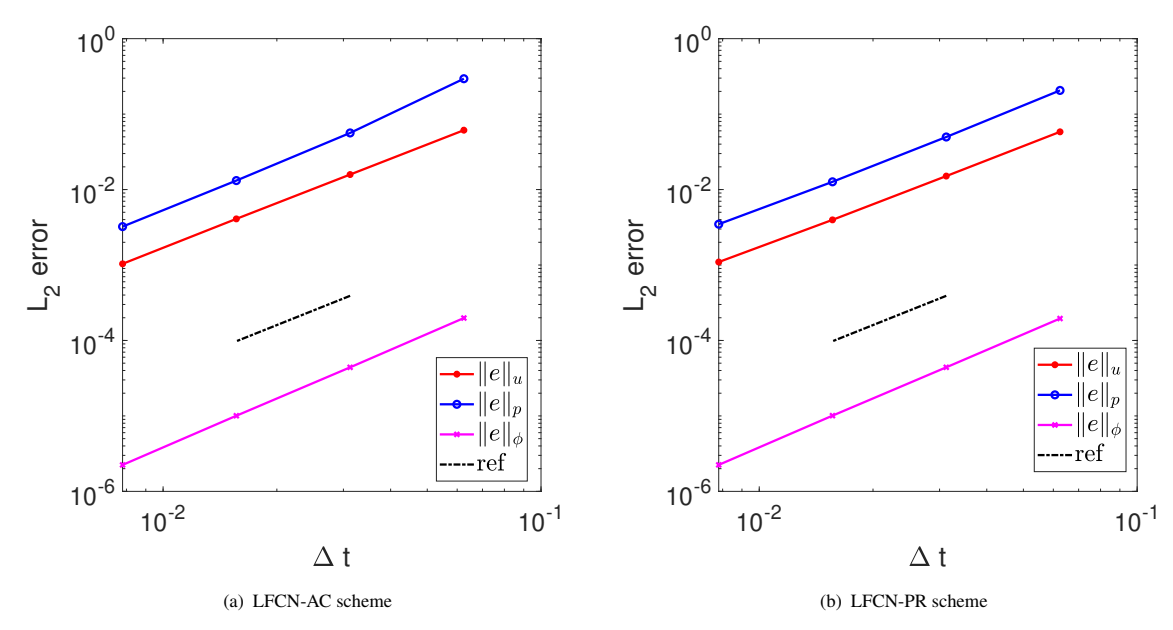


FIGURE 1 Log-Log plot of the error in L^2 norm with different time step size Δt .

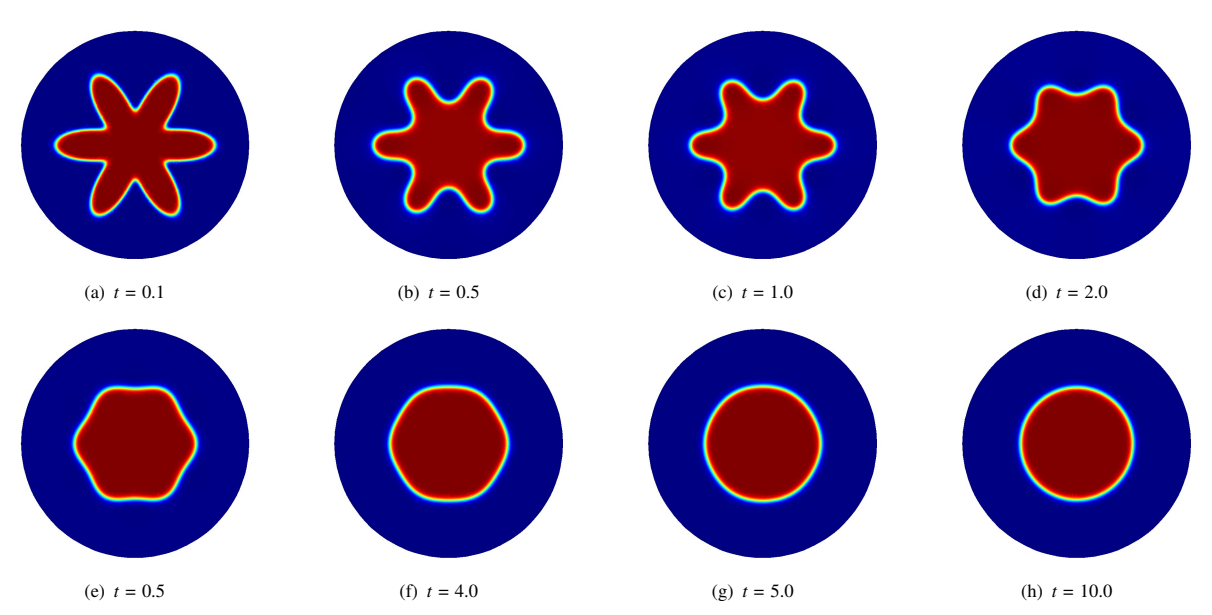


FIGURE 2 Shape relaxation of surface tension.

In this numerical test, we consider the spinodal decomposition on a complex domain to further validate the efficiency of the proposed CNLF scheme.

The computational domain is chosen as a ring domain $\Omega=\{(x,y)|0.3<\sqrt{(x-0.5)^2+(y-0.5)^2}<0.5\}$. The parameters are taken as same as in Example 2. Parameters are chosen as $ReDa=10^{-4},~\chi=1,~\frac{\nu}{\Pi}=100,~\epsilon=0.02,$ $We=100,~\gamma=0.01,~Pe=1,~m=0.01$, and $\alpha=2$ on The average of phase variable ϕ over the computational domain is approximately 0, for precisely, the initial value of ϕ is specified by $\phi_0=\bar{\phi}-0.05(2r(x)-1)$ with an average composition $\bar{\phi}=-0.05$ and random $r(x)\in[0,1]$. Time step size is taken $\Delta t=0.005$. The simulation is halted at time T=20. Figure A shows the evolution of phase variable for binary fluids. As we observed, the phase separation

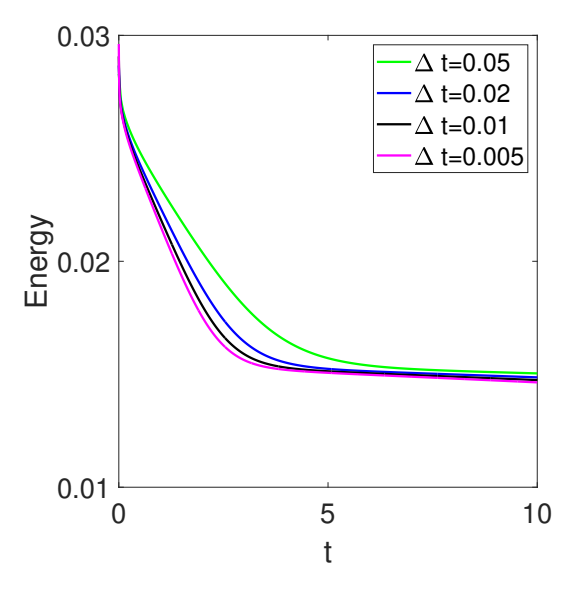


FIGURE 3 Evolution of the discrete energy for flower under surface tension with different time.

is well done through the domain is a complex ring. The expected simulation results illustrate the efficiency of our numerical method.

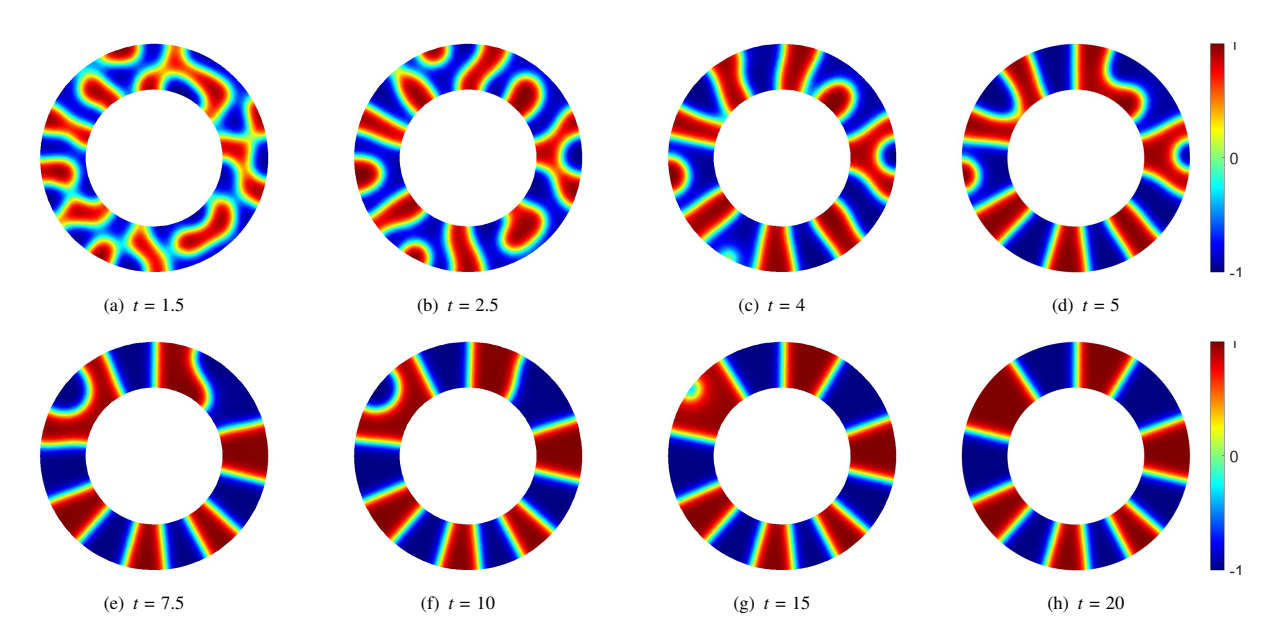


FIGURE 4 Snapshots of phase variable on a computational ring domain.

162

163

164

165

166

Example 4: Interface pinchoff in two and three dimensions.

In this test, we simulate the instability of fluid layers under Buoyancy-driven flow inside a Hele-Shaw cell⁴⁷. The physical problem is illustrated in Figure (5(a)), in which a lighter fluid layer is initially sandwiched by a heavy fluid layer. Under gravity, the upper interface is unstable, the heavier fluid flows downwards and penetrates the layer of light fluid. The lower interface is table and resits motion. Ultimately, the two interfaces meet and break up. To

perfectly capture the dynamics of the interface, we introduce the mesh adaptive technique in space taking advantage of the Galerkin finite element method.

The computational domain is a square domain $\Omega = [0, 2\pi] \times [0, 2\pi]$. Assuming the small difference in densities, the Boussinesq approximation is applied to CHD system. More precisely, the buoyancy-driven term $B := -\mathbf{g}\phi(\rho_1 - \rho_2)$ is added to the right side of Darcy equation (2.1b), here $\rho(\phi) = \frac{\rho_1 - \rho_2}{2}\phi + \frac{\rho_1 + \rho_2}{2}$, and \mathbf{g} is the gravitational acceleration with $\mathbf{g} = [0, \mathbf{g}]^T$.

The initial condition for order parameter is chosen as

$$\phi_0(x,y) = \frac{1}{2}\xi_+(x,y)\xi_-(x,y) - 1,\tag{5.2}$$

74 with

$$\xi_{\pm}(x,y) = 1 \pm \tanh\left(\frac{y - \pi \pm (0.5 + 0.1\cos(x))}{\sqrt{2}\epsilon}\right),$$

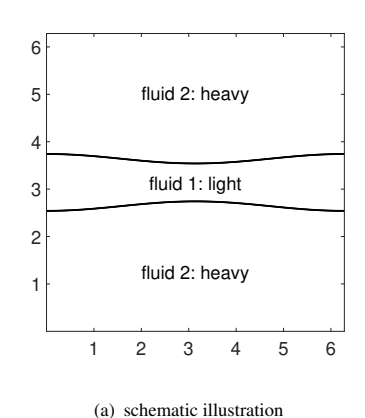
where $\phi=1$ is associated to the light fluid with density ρ_1 , and $\phi=-1$ is associated to the heavy fluid with density ρ_2 . The contour of initial phase variable is exhibited in Figure [5(b)]. We take parameters ReDa=0.005, $\chi=0.5$, $\Pi=0.66$, $\epsilon=0.05$, We=4, Pe=100, M=1, $\alpha=2$, $\alpha=1$, $\alpha=2$, $\alpha=1$, $\alpha=$

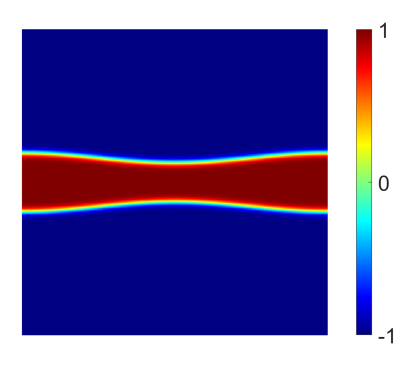
The characteristic snapshots of phase variable are reported in Figure 6 under g = 0.7365 for $\nu_1 : \nu_2 = 1 : 5$ and $\nu_1 : \nu_2 = 1 : 2.5$. We can clearly observe the rising of the bubble of light fluid, bridge rupture and the formation of satellite drops as expected. From Figures 6, we can observe that the small viscous ratio accelerates the dynamical process and leads to more satellite drops after rupture. The numerical results are very consistent with those reported in 19161724

We also simulate the interface pinch-off in three dimensions for binary fluids by setting the initial phase variable

$$\xi_{\pm}(x,y,z)=1\pm\tanh\left(\frac{4}{3\epsilon}\left(\sqrt{(z-\frac{1}{3})^2+(y-\frac{1}{3})^2}\pm\frac{1}{4\pi}\left(1+\frac{\cos(2\pi x)}{2}\right)\right)\right),$$

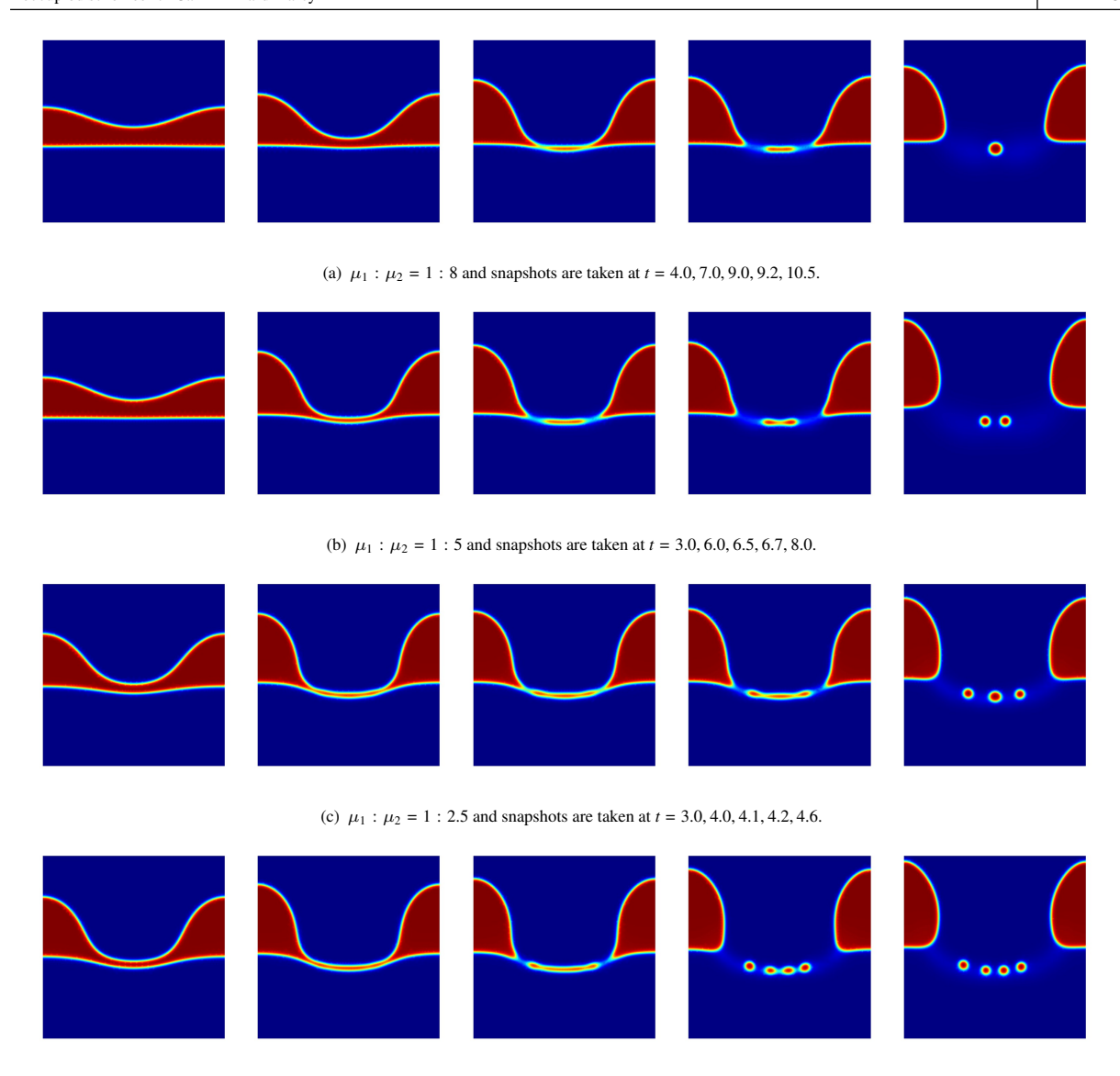
in computational domain $[0,1] \times [0,1] \times [0,1.5]$. The physical parameters are the same as in a two-dimensional case except for $\epsilon=0.03$. Taking g=0.7365, we draw the characteristic behaviors of iso-surface $\phi=0$ in Figure 7 at different times. We clearly observe the topology transition of the interface, light bubble actually arise after pinchoff. The ability to automatically capture topological changes verifies the effectiveness of the proposed numerical method proposed CNLF method.





(b) initial contour of ϕ_0

FIGURE 5 The configure of phase variable for the binary fluids.



(d) $\mu_1: \mu_2 = 1: 2$ and snapshots are taken at t = 3.0, 3.5, 3.7, 4.0, 4.2.

FIGURE 6 The topology transition of phase variable for interface pinchoff behavior with respect to different viscosity ratios under g = 0.7365.

Example 5: Viscous fingering with uniform injection.

190

191

192

193

194

195

We simulate the Saffman-Taylor instability to validate the effectiveness of our proposed CNLF method. The instability phenomenon also called viscous fingers, occurs when a less viscous fluid is invalided into a more viscous one, which significantly impacts the sweep efficiency of multiphase fluid through porous media.

Choose ReDa = 0.005, $\chi = 0.5$, $\Pi = 0.01$, $\epsilon = 1/128$, We = 540, Pe = 100, m = 0.001, $\alpha = 5$, $\Delta t = 0.0001$ and computational domain $\Omega = [0, 0.5] \times [0, 1.0]$. We consider different viscosities $\alpha(\phi) = \frac{\nu_1 - \nu_2}{2} \phi + \frac{\nu_1 + \nu_2}{2}$ corresponding to different viscous ratios under the absence of gravity. The initial conditions of the phase variable is given by

$$\phi_0(x,y) = -\tanh\left(\frac{4}{3\epsilon}\left(y - \frac{1}{10} + \frac{\cos(16\pi x)}{100}\right)\right)$$
 (5.3)

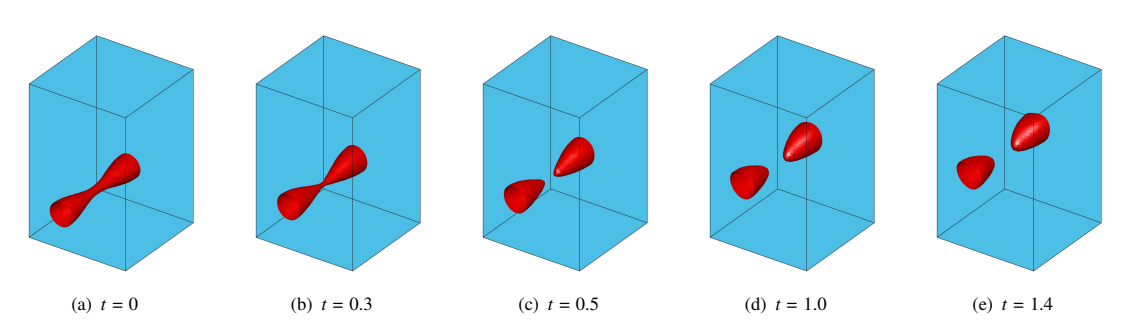


FIGURE 7 The topology transition of phase variable for interface pinchoff behavior in 3D at t = 0, 0.1, 0.2, 0.4, 0.6.

197

198

199

200

201

202

203

204

205

with a small perturbation on the fat interface between binary fluids. The boundary conditions for velocity are imposed, i.e. $u|_{y=0} = (0, v_{inj})$ with the uniform injected rate $v_{inj} = 50$ of less viscous fluid. Figure 8 exhibits the insurgency and elongation of the viscous finger phenomenon at different times.

We compared the length of fingers with different viscous ratios $\nu_1:\nu_2=1:5$, $\nu_1:\nu_2=1:10$ and $\nu_1:\nu_2=1:20$, and surface tension reported in Figure 8, which illustrates that the larger viscous ratio and small surface tension will pronounce the longer finger. The expected finger morphologies are in accord with the numerical results shown in [1619].

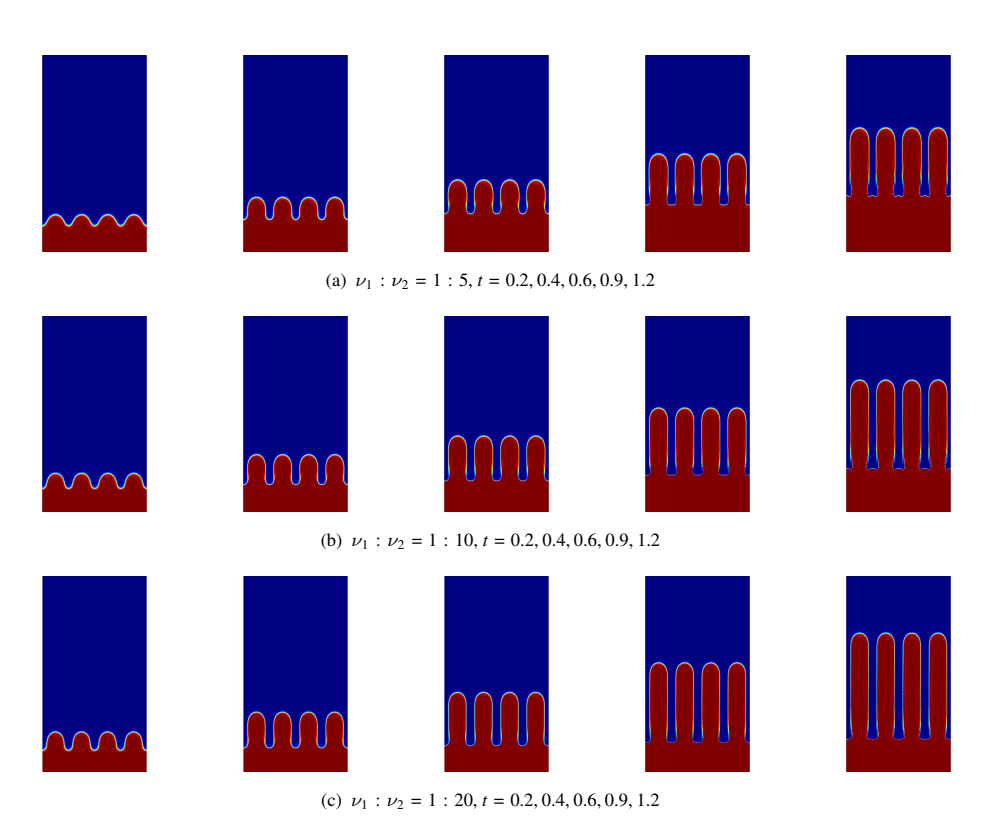


FIGURE 8 Snapshots of phase variable for viscous fingering with respect to different viscosity ratios.

Example 6: Rotational Hele-Shaw cell. We investigate the interface instability between two fluids under rotational Hele-Shaw cell, culminating in the appearance of finger patterns $\frac{48117}{2.1a}$. In the simulation, we apply the extra rotational force on the right side of momentum equation (2.1a). More precisely, the momentum equation is

replaced by the following formulation

$$\frac{ReDa}{\chi}\frac{\partial \boldsymbol{u}}{\partial t} + \nu(\phi)\Pi^{-1}\boldsymbol{u} + \nabla p + \frac{\epsilon^{-1}}{We}\phi\nabla\mu = C(1+\phi)(\omega^2\mathbf{r} + 2\omega(\mathbf{e}\times\boldsymbol{u})),$$

where $\mathbf{r} = (x - \pi, y - \pi)$, e = (0, 0, 1). The initial condition for phase variable are used

$$\phi_0(x, y) = -\tanh((\sqrt{(x-\pi)^2 + (y-\pi)^2} - R)/(\sqrt{2\epsilon}))$$
(5.4)

where $R = 1.3 + 0.002(1 + \cos(13\theta))$ and $\theta = \arctan(\frac{y-\pi}{x-\pi})$. The parameters are ReDa = 0.5, $\chi = 0.5$, $\epsilon = 0.035$, We = 10, Pe = 100, $m(\phi) = 1$, $\nu\Pi^{-1} = 20$, C = 7.5, $\omega = 2$ and $\Delta t = 0.001$. The deformation and evolution of finger patterns, their corresponding velocity field, and pressure are displayed in Figure Θ . We observed that on one hand, the pattern grows along the radial direction; on the other hand, the body appears to be rotated, exhibiting a distinct tilting of fingers at t = 0.6 and t = 0.8.

We also discuss the influence of different viscous ratios for the fingering pattern by using $\nu(\phi) = \frac{\nu_1 + \nu_2}{2} \phi + \frac{\nu_1 + \nu_2}{2}$ and $\Pi = 0.1$. The pattern morphology of finger dynamics are drawn in Figure 10 associated with $\nu_1 = 20$, $\nu = 15$ and $\nu_1 = 10$ under fixed $\nu_2 = 1$. From Figure 10, we can find that a smaller viscous ratio enhances the interfacial instability and finger competition dynamics. These numerical behaviors are in good agreement with the numerical findings obtained in 10

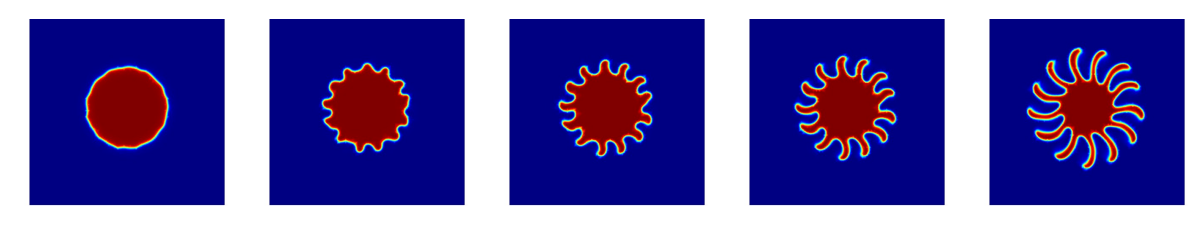


FIGURE 9 Snapshots of phase variable ϕ at t = 0.2, 0.4, 0.5, 0.6, 0.8 in a rotational Hele-Shaw cell

6 | CONCLUSIONS

In this paper, we propose a second-order Crank-Nicolson leap-frog scheme for numerically studying Cahn-Hilliard-Darcy model, which describes two-phase flow in porous medium or a Hele-Shaw cell. We exploited the artificial compression method and pressure projection method to achieve the totally decoupled of phase variable, pressure and velocity. Therefore, the designed CNLF-AC and CNLF-PR numerical methods are totally decoupled, linearized, second-order and energy stable. We rigorously prove the unconditionally stability for both CNLF-AC and CNLF-PR time stepping numerical scheme. In order to efficiently capture the interface between binary fluids, we use the Galerkin finite element method in space to obtain the fully discretization. The typical numerical tests are given to validate the accuracy and efficiency. Several interesting phenomenon are simulated to illustrate the robustness of the developed CNLF method, including spinodal decomposition in complex domain, interface singularities during topology transition, and viscous fingers in unform injection and rotational Hele-Shaw cell.

REFERENCES

- 1. Saffman PG, Taylor G. The penetration of a fluid into a porous medium or Hele-Shaw cell containing a more viscous liquid. *Proc. Roy. Soc. London. Ser. A.* 1958;245:312–329. (2 plates).
- 2. Homsy GM. Viscous Fingering in Porous Media. Ann. Rev. Fluid Mech.. 1987;19:277-311.
- 3. Wise S, Lowengrub J, Frieboes H, Cristini V. Three-dimensional multispecies nonlinear tumor growth-I model and numerical method. *J. Theor. Biol.*. 2008;253(3):524-543.
- 4. Zhang M, Maxworthy T. The interactive dynamics of flow and directional solidification in a Hele-Shaw cell Part I. Experimental investigation of parallel shear flow. *J. Fluid Mech.*. 2002;470:247-268.

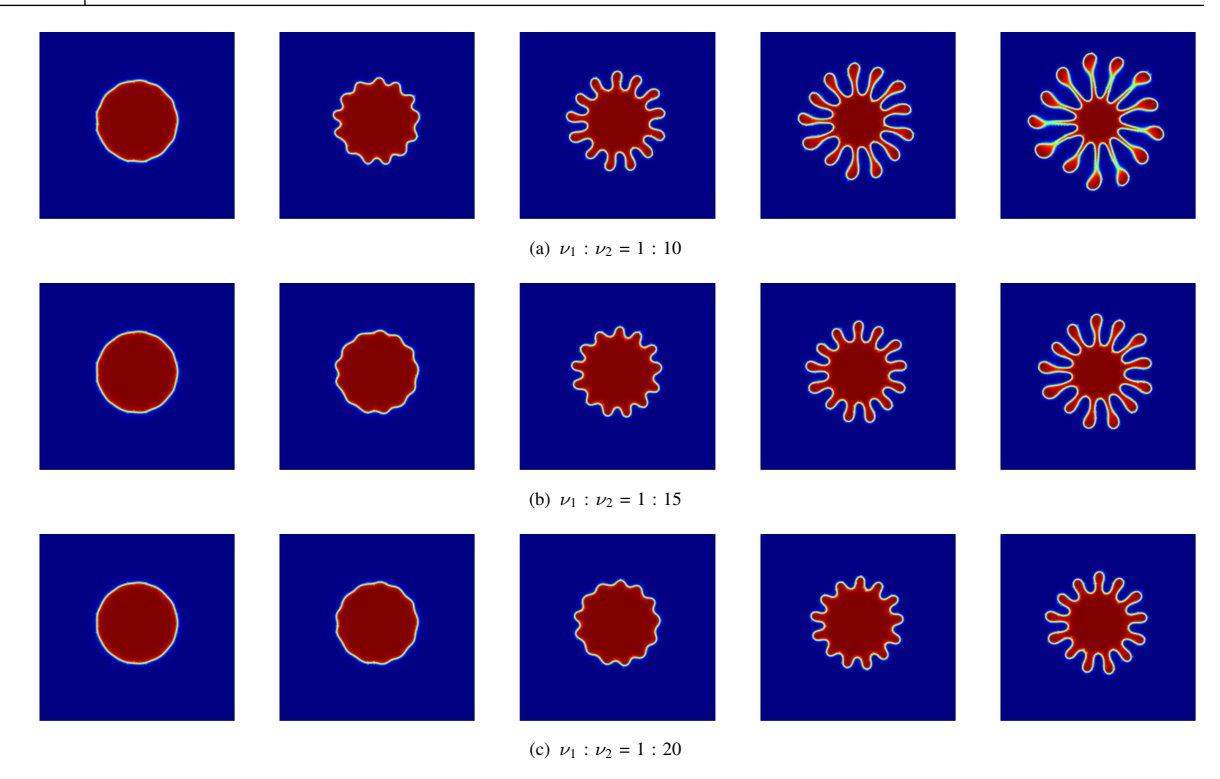


FIGURE 10 Snapshots of phase variable with respect to different viscosity ratios at t = 0.3, 0.6, 0.9, 1.2, 1.5.

- Lu HW, Glasner K, Bertozzi IA, Kim CJ. A diffuse-interface model for electrowetting drops in a Hele-Shaw cell. J. Fluid Mech.. 2007;590:411-435.
- Chono S, Tsuji T, Sun J. Numerical Simulation of Molding Hele-Shaw Flow of Polymeric Liquid Crystals. *Journal of Fluid Science and Technol.*, 2007;2(2):368-379.
- 7. Glasner K. A Diffuse Interface Approach to Hele-Shaw Flow. Nonlinearity. 2003;16:49-66.

237

238

239

240

241 242

243

244

245

246

247 248

249

250

251

252

253 254

255

256

257

266

267

- 8. Han D, Sun D, Wang X. Two-phase flows in karstic geometry. Math. Methods Appl. Sci.. 2014;37(18):3048-3063.
- 9. Ganesan V, Brenner H. A diffuse interface model of two-phase flow in porous media. R. Soc. Lond. Proc. Ser. A Math. Phys. Eng. Sci.. 2000;456(1996):731–803. doi: 10.1098/rspa.2000.0537
- 10. Schmuck M, Pradas M, Pavliotis GA, Kalliadasis S. Upscaled phase-field models for interfacial dynamics in strongly heterogeneous domains. *Proc. R. Soc. Lond. Ser. A Math. Phys. Eng. Sci.*. 2012;468(2147):3705–3724. doi: 10.1098/rspa.2012.0020
- Schmuck M, Pradas M, Pavliotis GA, Kalliadasis S. Derivation of effective macroscopic Stokes-Cahn-Hilliard equations for periodic immiscible flows in porous media. *Nonlinearity*. 2013;26(12):3259–3277.
- 12. Daly KR, Roose T. Homogenization of two fluid flow in porous media. *Proc. A.*. 2015;471(2176):20140564. doi: 10.1098/rspa.2014.0564
- 13. Chen J, Sun S, Wang X. Homogenization of two-phase fluid flow in porous media via volume averaging. *Journal of Computational and Applied Mathematics*. 2019;353:265-282. doi: https://doi.org/10.1016/j.cam.2018.12.023
- 14. Lee H, Lowengrub J, Goodman J. Modeling pinchoff and reconnection in a Hele-Shaw cell. I. The models and their calibration. *Phys. Fluids.* 2002;14(2):492-513.
- 15. Cueto-Felgueroso L, Juanes R. A phase-field model of two-phase Hele-Shaw flow. J. Fluid Mech.. 2014;758:522-552.
- Dedè L, Garcke H, Lam K. A Hele-Shaw-Cahn-Hilliard model for incompressible two-phase flows with different densities. J. Math. Fluid Mech.. 2018;20(2):531-567.
- 258 17. Yang J, Kim J. An efficient stabilized multiple auxiliary variables method for the Cahn-Hilliard-Darcy two-phase flow system.
 Comput. Fluids. 2021;223:104948.
- 18. Yang X. On a novel fully-decoupled, linear and second-order accurate numerical scheme for the Cahn-Hilliard-Darcy system of two-phase Hele-Shaw flow. *Comput. Phys. Commun.*. 2021;263:107868.
- Han D, Wang X. A Second Order in Time, Decoupled, Unconditionally Stable Numerical Scheme for the Cahn-Hilliard-Darcy
 System. J. Sci. Comput.. 2018;77(2):1210-1233.
- Han D, Wang X. Decoupled energy-law preserving numerical schemes for the Cahn-Hilliard-Darcy system. *Numer. Methods Partial Differential Equations*. 2016;32(3):936-954.
 - 21. Feng X, Wise S. Analysis of a Darcy-Cahn-Hilliard diffuse interface model for the Hele-Shaw flow and its fully discrete finite element approximation. *SIAM J. Numer. Anal.*. 2012;50(3):1320-1343.
- 22. Gao Y, He X, Nie Y. Second-order, fully decoupled, linearized, and unconditionally stable scalar auxiliary variable schemes for
 Cahn-Hilliard-Darcy system. *Numer. Methods Partial Differential Eq.*. 2022;38:1658-1683.

- 23. Guo R, Xia Y, Xu Y. An efficient fully-discrete local discontinuous Galerkin method for the Cahn-Hilliard-Hele-Shaw system. *J. Comput. Phys.*. 2014;264:23-40.
- 272 24. Li Y, Yu W, Zhao J, Wang Q. Second order linear decoupled energy dissipation rate preserving schemes for the Cahn-Hilliard-273 extended-Darcy model. *J. Comput. Phys.*. 2021;444:110561.
- 274 25. Chen R, Li Y, Pan K, Yang X. Efficient second-order, linear, decoupled and unconditionally energy stable schemes of the Cahn-Hilliard-Darcy equations for the Hele-Shaw flow. *Numer. Math.*. 2022;92:2275-2306.
- 26. Wu K, Huang F, Shen J. A new class of higher-order decoupled schemes for the incompressible Navier-Stokes equations and applications to rotating dynamics. *J. Comput. Phys.*. 2022;458:111097. doi: 10.1016/j.jcp.2022.111097
- 273. Jiang M, Zhang Z, Zhao J. Improving the accuracy and consistency of the scalar auxiliary variable (SAV) method with relaxation. *J. Comput. Phys.*. 2022;456:110954. doi: 10.1016/j.jcp.2022.110954
- 28. Layton W, Trenchea C. Stability of two IMEX methods, CNLF and BDF2-AB2, for uncoupling systems of evolution equations.

 Appl. Numer. Math.. 2012;62(2):112-120.
- 29. DeCaria V, Layton W, McLaughlin M. A conservative, second order, unconditionally stable artificial compression method. *Comput. Methods Appl. Mech. Engrg.*. 2017;325:733-747.
- 284 30. Jiang N, Li Y, Yang H. A conservative, second order, unconditionally stable artificial compression method. SIAM J. Numer. Anal..
 285 2021;59(1):401-428.
- 286 31. Han D, Jiang N. A second order, linear, unconditionally stable, Crank-Nicolson-Leapfrog scheme for phase field models of two-phase incompressible flows. Appl. Math. Lett.. 2020;108:106521.
- 288 32. Chen L, Zhao J. A novel second-order linear scheme for the Cahn-Hilliard-Navier-Stokes equations. *J. Comput. Phys.*. 2020;423:109782. doi: 10.1016/j.jcp.2020.109782
- 290 33. Qian L, Wu C, Cai H, Feng X, Qiao Y. A fully-decoupled artificial compressible Crank-Nicolson-Leapfrog time stepping scheme for the phase field model of two-phase incompressible flows. *J. Sci. Comput.*. 2023;94:50.
- 292 34. Li Y, Yu Q, Fang W, Xia B, Kim J. A stable second-order BDF scheme for three dimensional Cahn-Hilliard-Hele-Shaw system. *Adv. Comput. Math.*. 2021;47(3):1-18.
- 294 35. Han D. A Decoupled Unconditionally Stable Numerical Scheme for the Cahn-Hilliard-Hele-Shaw System. *J. Sci. Comput.*. 2016;66(3):1102-1121.
- 296 36. Gao Y, Li R, Mei L, Lin Y. Second-order order decoupled energy stable numerical scheme for Cahn-Hilliard-Hele-Shaw system.
 297 Appl. Numer. Math.. 2020;157:338-355.
- 298 37. DeCaria V, Illiescu T, Layton W, McLaughlin M, Schneier M. An artificial compression reduced order model. *SIAM J. Numer. Anal.*. 299 2020;58:565-589.
- 38. Guermond JL, Minev P. High-order time stepping for the Navier-Stokes equations with minimal computational complexity. *J. Comput. Appl. Math.*. 2017;310:92-103.
- 39. Kan vJ. A second-order accurate pressure-correction scheme for viscous incompressible flow. SIAM J. Sci. Stat. Comput.. 1986;7(3):870-891.
- 40. Guermond JL, Minev P, Shen J. Error Analysis of Pressure-Correction Schemes for the Time-Dependent Stokes Equations with Open Boundary Conditions. *SIAM J. Numer. Anl.*. 2005;43(1):239-258.
- 41. Guermond JL, Salgado A. A splitting method for incompressible flows with variable density based on a pressure Poisson equation. *J. Comput. Phys.*. 2009;228(8):2834-2846.
- 42. Liu Y, Chen W, Wang C, Wise S. Error analysis of a mixed finite element method for a Cahn-Hilliard-Hele-Shaw system. *Numer.*Math.. 2017;135(3):679-709.
- 43. Chen W, Liu Y, Wang C, Wise SM. Convergence analysis of a fully discrete finite difference scheme for the Cahn-Hilliard-Hele-Shaw equation. *Math. Compt.*. 2016;85(301):2231-2257.
- 44. Chen W, Wang S, Zhang Y, Han D, Wang C, Wang X. Error estimate of a decoupled numerical scheme for the Cahn-Hilliard-Stokes-Darcy system. *IMA Numer. Analysis.* 2021;26(1-2):1-34.
- 45. Wang C, Wang J, Xia Z, Han D, , Xu L. Optimal error estimates of a Crank-Nicolson finite element projection method for magnetohydrodynamic equations. *ESAIM Math. Model. Numer. Anal.*. 2022;56(3):769-787.
- 46. Cai W, Sun W, Wang J, Yang Z. Optimal *L*² Error Estimates of Unconditionally Stable Finite Element Schemes for the Cahn-Hilliard-Navier-Stokes System. *SIAM J. Numer. Anal.*. 2023;61(3):1218-1245.
- 47. Sun Y, Beckermann C. A two-phase diffuse-interface model for Hele-Shaw flows with large property contrasts. *Physica D*. 2008;237:3089-3098.
- 48. Chen CY, Huang YS, Miranda J. Diffuse-interface approach to rotating Hele-Shaw flows. *Phys. Rev. E.* 2011;84:046302.